










Extra lithium-ion storage capacity enabled by liquid-phase exfoliated indium selenide nanosheets conductive network†

Chuanfang (John) Zhang, *^a Meiyang Liang,^{bc} Sang-Hoon Park,^{bc} Zifeng Lin, ^d Andrés Seral-Ascaso,^{bc} Longlu Wang, ^e Amir Pakdel, ^{bc} Cormac Ó Coileáin,^{bc} John Boland,^{bf} Oskar Ronan,^{bc} Niall McEvoy, ^{bc} Bingan Lu, ^e Yonggang Wang, ^g Yongyao Xia, ^g Jonathan N. Coleman *^{bf} and Valeria Nicolosi*^{bc}

As a recent addition to the family of van der Waals layered crystals, indium selenide (InSe) possesses unique optoelectronic and photonic properties, enabling high-performance electronic devices for broad applications. Nevertheless, the lithium storage behavior of InSe flakes is thus largely unexplored due to its low electronic conductivity and challenges associated with its exfoliation. Here, we prepare few-layered InSe flakes through liquid-phase exfoliation of wet-chemistry-synthesized layered InSe single crystals, and percolate the flakes with carbon nanotube (CNT) networks in order to form flexible anodes to store lithium (Li). We demonstrate, with the support of CNTs, that exfoliated InSe flakes possess superior Li storage capacity to bulk InSe; the capacity increases over prolonged cycling up to 1224 mA h g⁻¹ from 520 mA h g⁻¹, coupled with excellent rate handling properties and long-term cycling stability. The operando X-ray diffraction results suggest that the alloying of indium with Li dominates the Li storage reactions. By combining with density-functional theory calculations and post-mortem analysis, we believe that the *in situ* formed indium gradually reduces the domain size, forming nanoclusters which allow the accommodation of 4 Li⁺ per atomic indium, and leading to extra capacity beyond the traditional theoretical value. This new “nanocluster alloying” Li storage mechanism may inspire new architectures or methods to synthesize few-layered InSe, thereby presenting broad opportunities for high-performance Li-ion battery anode technologies.

Introduction

The rapid development of smart, portable electronic devices has greatly stimulated the research on advanced energy storage

devices^{1–3} such as Li-ion batteries (LIBs) with superior capacity and long cycle life.^{4–11} Graphite, the standard commercial anode material, which typically suffers from low capacity (~374 mA h g⁻¹) and low charge-discharge rate (sluggish ion diffusion kinetics, 10⁻¹¹–10⁻¹⁰ cm² s⁻¹) due to the intercalation mechanism, cannot meet the ever-increasing energy/power demands.^{12,13} To this end, the search for novel anode materials with non-intercalation Li storage mechanisms and large theoretical capacity, such as materials with lithiation conversion and/or alloy reactions,¹⁴ has benefited from intense interest. Two-dimensional (2D) layered metal chalcogenides (MC, where M is Ga/In, C is S/Se/Te, etc.) possess exotic properties and multi-valences,^{15,16} enabling a variety of conversion/alloy reactions with lithium, and thus are considered as promising candidates for next-generation battery anode materials.

As a member of the MC family, layered indium selenide (InSe) crystals consist of strong in-plane covalently bonded Se–In–In–Se layers that interact weakly in the out-of-plane direction *via* van der Waals forces.¹⁷ As such, layered InSe

^a Swiss Federal Laboratories for Materials Science and Technology (Empa), ETH Domain, Überlandstrasse 129, CH-8600, Dübendorf, Switzerland.

E-mail: chuanfang.zhang@empa.ch

^b CRANN and AMBER research centers, Trinity College Dublin, Dublin 2, Ireland.

E-mail: colemaj@tcd.ie, nicolov@tcd.ie

^c School of Chemistry, Trinity College Dublin, Dublin 2, Ireland

^d College of Materials Science and Engineering, Sichuan University, Chengdu 610065, P. R. China

^e School of Physics and Electronics, Hunan University, Changsha 410082, P. R. China

^f School of Physics, Trinity College Dublin, Dublin 2, Ireland

^g Department of Chemistry, Shanghai Key Laboratory of Catalysis and Innovative Materials, Center of Chemistry for Energy Materials, Fudan University, Shanghai, 200433, China

† Electronic supplementary information (ESI) available. See DOI: 10.1039/d0ee01052a

allows the efficient exfoliation (either micro-mechanical or liquid-phase exfoliation) of bulk crystals into few-layered flakes.¹⁶ Such a thinning process switches the direct bandgap (~ 1.3 eV) to an indirect bandgap (~ 3.0 eV) that has been confirmed in atomically thin flakes,^{18–20} coupled with excellent charge carrier mobility (up to 10^3 cm² V⁻¹ s⁻¹), quantum Hall effect and other anomalous optical responses at room temperature.¹⁷ As such, few-layered InSe has been widely applied in electronic and optoelectronic devices such as transistors (on/off ratio up to 10^8)^{21,22} and photodetectors (photoresponsivities up to 10^6 A W⁻¹).^{23,24}

Nevertheless, the potential application of layered InSe in LIBs remains relatively unexplored, partially due to its poor electrical conductivity as well as sluggish Li⁺ diffusion kinetics in its bulk structure.²⁵ While incorporating bulk InSe into a conductive matrix (such as carbon black²⁶) effectively improves the electron transport kinetics, the ion accessible sites in bulk InSe are still limited. On the other hand, the conversion-alloy reaction mechanism results in huge volume change for InSe upon repeated cycling, which inevitably leads to the disconnection of the active material from conductive agents, followed by a quick capacity decay.^{26–28} For example, Fu *et al.* reported an initial capacity of 595 mA h g⁻¹ in their InSe thin-film electrode which quickly decayed to 410 mA h g⁻¹ after 10 cycles.²⁹ While fabricating InSe nano/micro-structures improves the reversible capacity up to 650 mA h g⁻¹, the electrodes still suffers from poor cycling (40 cycles).²⁷ To encapsulate the issue, engineering InSe electrodes with abundant active sites for efficient Li⁺ diffusion while assimilating the stress from the repeated volume expansion/contraction is expected to result in battery anodes with both high capacity and long cycle-life, but this has proven quite challenging. In addition, the absence of a scalable preparation route for InSe flakes also limits their technological potential.

In this context, liquid-phase exfoliation (LPE) of layered materials in suitable solvents has been demonstrated as a viable method to give large-scale 2D nanosheet at low costs, enabling efficient solution processing of thin films, composites and devices.^{15,30,31} Colloidal solutions enriched with few-layered graphene,³⁰ molybdenum disulfide,³² black phosphorus,³³ gallium sulfide and selenide,^{34,35} *etc.* have been reported; these few-layered 2D nanosheets possess abundant active sites, thus exhibiting much enhanced electrochemical and catalytic properties compared to those of their bulk counterpart.^{34–38} This suggests the potential utility of LPE for InSe to synthesize few-layered flakes for the LIB anodes. Although liquid-phase exfoliated InSe was reported for hydrogen evolution¹⁹ and photodetectors,²⁰ to the best of our knowledge, there are no reports demonstrating such material employed for high-capacity LIB anode with excellent cycling stability.

Herein, we report on few-layered InSe/carbon nanotube (FL-InSe/CNT) flexible thin films as a high-performance LIB anode material. FL-InSe flakes are liquid-phase exfoliated from the wet-chemistry-synthesized β -InSe single crystals, and percolated with high-aspect-ratio CNTs to form a conductive percolated network. We confirm high capacity in the FL-InSe/CNT thin film electrode that increases from 520 mA h g⁻¹ to

1224 mA h g⁻¹ after 245 cycles, coupled with $\sim 97\%$ coulombic efficiency, excellent rate handling and cycling performance. Such excellent electrochemical performance is ascribed to the excellent mechanical strength of the CNT porous network, as well as a new “nanocluster-alloying” Li storage mechanism, as revealed by the *in situ* X-ray diffraction (XRD) and density-function theory (DFT) calculation results. We believe that the LPE-based straightforward approach to fabricate FL-MC/conductive porous scaffold combining with the new Li storage mechanism can be generalized to other layered materials, which may inspire new electrode architectures with superior charge storage properties, thus enabling a wide range of applications such as in wearable electronics, energy storage devices and optoelectronic.

Results and discussion

We begin with the wet synthesis of layered InSe. Through employing a long-chain primary alkylamine (a solution mixture of hexadecylamine and dodecylamine) as the solvent and reductant, the indium acetate (In(CH₃COO)₃) was thermolytically reduced and decomposed into In species at elevated temperature.³⁹ Selenium powder which typically possesses a poor solubility in amines such as oleylamine at < 205 °C,⁴⁰ dissolved rapidly in the hot medium at 300 °C, ensuring the efficient solution-controlled growth of InSe domain. Previous reports suggest that the Se/In stock ratio heavily affects the morphology and crystal structure of the resultant InSe domain.⁴¹ Here, hexagonal InSe is believed to possess type-A edge and type-B edge, where the coordination rates of incoming Se and In atoms are different (Fig. 1a). A higher Se/In stock ratio ensures saturated Se coordination rate at both edges of the InSe nuclei. Consequently, the coordination rate of In, which is faster along type-A edge,⁴¹ governs the growth rate of the InSe domain, leading to the formation of triangular InSe. When the Se/In stock ratio is decreased below the saturation condition, the coordination rate of Se and In alternatively control the domain growth rate along type-B and type-A, respectively, resulting in the formation of hexagonal InSe domains.⁴¹ Upon aging, hexagonal InSe domains assemble into layered crystals, as demonstrated in Fig. 1a. Here we used a Se/In stock ratio < 1 to ensure the as-formed InSe crystals were predominantly hexagonal.

Such a self-confined synthesis assisted by the mixture of amines represents a straightforward route to high-quality layered InSe semiconductors. This is evidenced by the scanning electron microscopy (SEM) images in Fig. 1b and Fig. S1a, b (ESI[†]), where hexagonal layered crystals with uniform lateral size are observed. Through statistical analysis based on the SEM images, these crystals possess a mean lateral size of $\langle L \rangle = 470 \pm 8$ nm, according to the size distribution histogram in Fig. S1c (ESI[†]). Transmission electron microscopy (TEM) and atomic force microscopy (AFM) images (Fig. S2a–c, ESI[†]) further suggest the shape of hexagonal InSe crystals, which are ~ 110 nm in thickness according to the height profile (Fig. S2d, ESI[†]). The XRD pattern in Fig. 1c indicates that the as-synthesized crystals

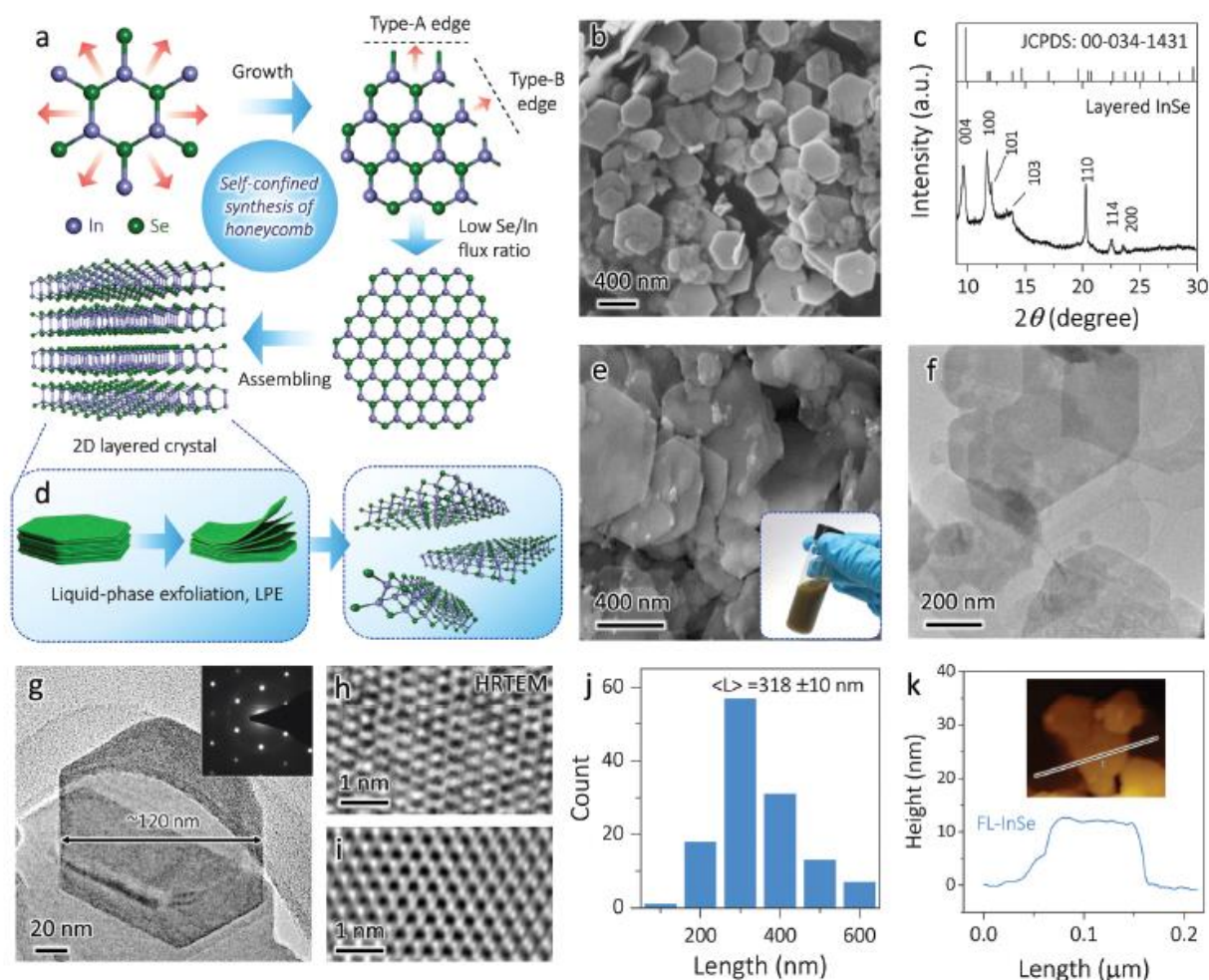


Fig. 1 (a) Schematic of growth of layered hexagonal InSe crystals through a wet-chemistry approach. (b) SEM image and (c) XRD pattern of as-synthesized hexagonal layered InSe crystal. (d) Scheme of liquid-phase exfoliation of FL-InSe. (e) SEM image and (f and g) TEM images of FL-InSe flakes at different magnifications. Inset in (g) is the SAED pattern, showing a hexagonal atomic structure in the flakes. (h) HRTEM and (i) flow-pass filtered version of image of FL-InSe flakes, showing a highly crystalline structure. (j) Size distribution and (k) height profile of exfoliated InSe flakes. Inset in (k) profile from typical AFM image.

are hexagonal $P6_3/mmc$ InSe ($a = 4.02 \text{ \AA}$, $c = 16.8 \text{ \AA}$, JCPDS card no. 00-034-1431).⁴¹

In order to obtain FL-InSe flakes, the layered InSe crystals were bath-sonicated in *N*-methyl-2-pyrrolidone (NMP), whose Hansen solubility parameters and surface energy are suitable for most 2D layered materials.^{15,42} Such a LPE typically employs sonic energy or shear force to overcome the weak van der Waals coupling of the layers and delaminate into few-layered nanosheets, as schematically demonstrated in Fig. 1d. After exfoliation, the resultant nanosheets were transferred to isopropanol (IPA), forming environmentally friendly colloidal solutions (inset of Fig. 1e) with concentration up to 5 mg mL^{-1} . SEM images confirm the presence of FL-InSe with a broad lateral size distribution (Fig. 1e and Fig. S3a, ESI[†]). This is expected and normally occurs due to the “scissor effect” during LPE.^{34,35} TEM images indicate plenty of exfoliated flakes with well-defined edges and no apparent damage in the basal plane (Fig. 1f, g and Fig. S3b, c, ESI[†]), suggesting the exfoliated material is of high quality. This is further verified by the selected area electron diffraction (SAED, inset of Fig. 1g),

high-resolution TEM (HRTEM, Fig. 1h) and flow-pass filtered version of image (Fig. 1i) where hexagonal lattice symmetry is observed in the exfoliated InSe flakes with a highly-crystalline structure. These exfoliated flakes possess a mean lateral size of $\langle L \rangle = 318 \pm 10 \text{ nm}$ (Fig. 1j) and a much smaller thickness ($\sim 10 \text{ nm}$) compared to that of bulk InSe after exfoliation, according to the size histogram and AFM/height profile (Fig. 1k), respectively. Nevertheless, the crystal structure of hexagonal InSe was well-maintained (Fig. S4, ESI[†]); no apparent defects were introduced to the exfoliated InSe flakes during sonication, best evidenced by the almost identical X-ray photoelectron spectroscopy (XPS) spectra in Fig. S5 (ESI[†]).

Next, the FL-InSe flakes were percolated with CNTs by vacuum filtration of their mixed dispersions, forming binder-free flexible thin films, as shown in Fig. 2a. As references, control samples including Layered InSe, Layered InSe/CNT, FL-InSe films were also filtrated with similar thickness ($\sim 3 \mu\text{m}$). TEM image indicates that bundles and apparent defects are found on the as-obtained carbon nanotube walls, which are

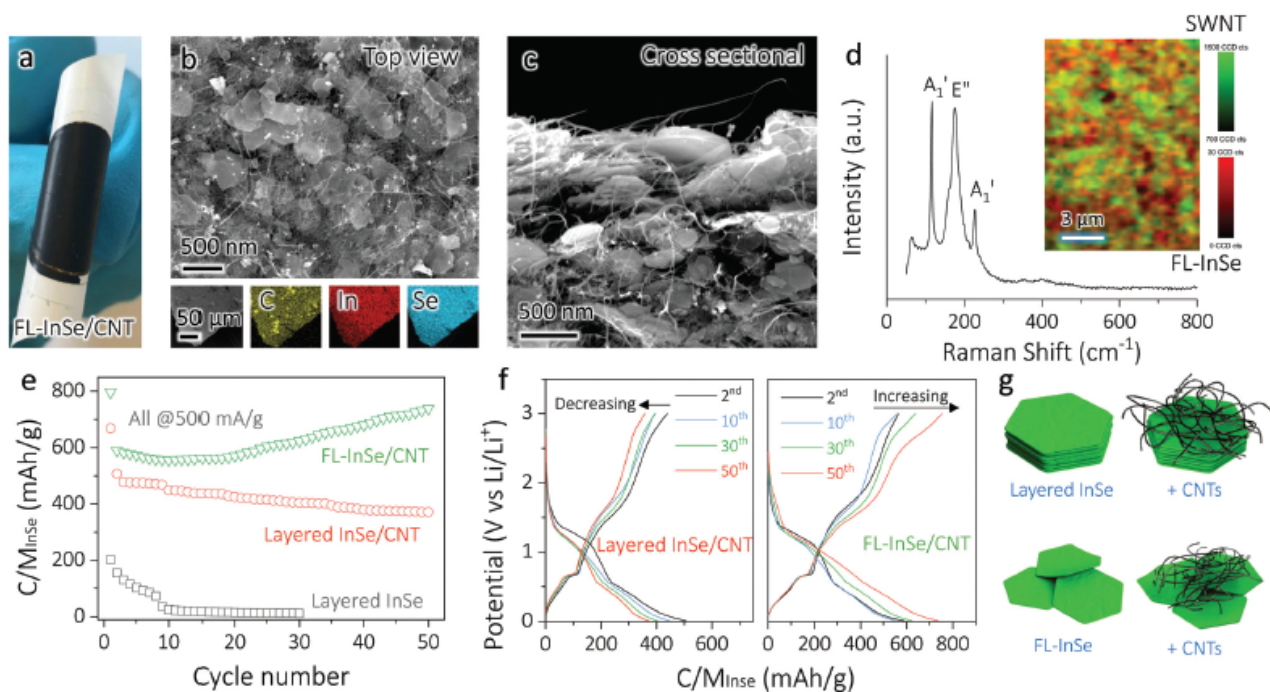


Fig. 2 (a) Optical image of flexible FL-InSe/CNT thin film supported on the filtering membrane. (b) Top-view and (c) cross sectional SEM images of FL-InSe/CNT film, showing a homogeneous distribution of FL-InSe flakes among the percolated CNT network, as shown in the EDX mapping in (b). (d) Raman spectrum of FL-InSe flakes. Inset is overlaid mapping of InSe A_1' and CNT G band sum, indicating uniform mixing of the two phases. (e) Capacity per InSe in different films over 50 cycles at 500 mA g^{-1} . (f) GCD profiles of layered InSe/CNT and FL-InSe/CNT at different cycles, showing the importance of exfoliated InSe flakes percolated in conductive network in achieving high capacity anode material by boosting the accessible sites to CNTs and electrolyte, as shown in (g).

quite typical for CNTs (Fig. S6, ESI[†]). Top-view and cross-sectional SEM images of a typical sample (20 wt% CNT, labeled as FL-InSe/CNT for further studies unless specifically noted) indicate that the FL-InSe flakes are uniformly embedded in the CNT percolated network (Fig. 2b, c and Fig. S7a, b, ESI[†]). Such a homogeneous distribution of both CNTs and FL-InSe flakes is also confirmed by elemental mapping of In, Se and C, according to energy-dispersive X-ray spectroscopy (EDX) mapping in the SEM (Fig. 2b and Fig. S7c, ESI[†]). The Raman spectrum of FL-InSe/CNT in Fig. 2d indicates characteristic lattice vibrations at ~ 116 , ~ 176 and $\sim 227 \text{ cm}^{-1}$, corresponding to the InSe A_1' , E'' , and A_1' modes, respectively.⁴³ The color-coded map, showing contributions from both CNTs and FL-InSe flakes based on the Raman spectrum, also implies the flexible thin film is uniform (inset of Fig. 2d). We believe the homogeneous distribution of FL-InSe flakes among the CNT percolated conductive network not only forms sufficient voids for rapid Li^+ diffusion as well as volume expansion, but also promotes electron transport pathways for better rate handling properties, as discussed below.

Electrochemical performance, including cyclic voltammogram (CV) and galvanostatic charge–discharge (GCD) tests of various samples were conducted. A strong cathodic peak centered at 1.17 V (vs. Li/Li^+) is observed in the first cycle CV curve of the Layered InSe/CNT electrode, which disappears in the subsequent cycles (Fig. S8a, ESI[†]), suggesting the composite possibly undergoes structural change as well as the formation

of solid electrolyte interphase (SEI).⁴⁴ Locations of other cathodic and anodic peaks are well defined and agree with previous reports on InSe thin films.²⁵ The Layered InSe/CNT electrode exhibits an initial capacity up to 970 mA h g^{-1} at 100 mA g^{-1} , and decreases to 428 mA h g^{-1} after 5 cycles (Fig. S8b and c, ESI[†]), similar to those of InSe thin films with different structures.^{25,27} At 500 mA g^{-1} , the FL-InSe/CNT electrode showcases an initial capacity of $\sim 797 \text{ mA h g}^{-1}$ while layered InSe/CNT exhibits an initial capacity of $\sim 669 \text{ mA h g}^{-1}$ (Fig. 2e). After 10 cycles, the capacity of FL-InSe/CNT electrode gradually increases and reaches 740 mA h g^{-1} per InSe after 50 cycles (Fig. 2e and f). This could be possibly explained by the differences on the electrode structure. While bulk InSe crystals are percolated with CNTs, both the Li^+ diffusion and electron transport kinetics within the layered thick flakes are sluggish. On the other hand, FL-InSe flakes increase the chance of full contact with CNTs by exposing thinner sheets to the conductive network, leading to much enhanced InSe utilization and improved capacity and cycling, as schematically illustrated in Fig. 2g.

To better understand the conductivity effect, we fabricated a series of FL-InSe/CNT films with different CNT mass fractions while similar in thickness, and evaluated their electrical and electrochemical properties. As shown in Fig. 3a (top panel), adding 30 wt% CNTs dramatically improves the in-plane conductivity up to 560 S m^{-1} from 0.3 S m^{-1} for 5 wt% CNT composite. The scaling of electrical conductivity of the

composites can be well fitted and interpreted using percolation theory:⁴⁵

$$\sigma_{IP} \propto (M_f - M_{f,c})^n \quad (1)$$

where σ is the in-plane electrical conductivity, M_f is CNT mass fraction, $M_{f,c}$ is CNT fraction threshold to form the first conductive paths and n is the conductivity exponent.⁴⁵ While CNT volume fraction is frequently used when plotting the results, it is still reasonable to make appropriate analysis using the mass fraction, since the latter scales closely with volume fraction. The good fitting gives a $n = 2.7$ and a percolation threshold of ~ 1 wt% in the FL-InSe/CNT composites, very similar to numbers achieved for MoS₂/SWCNT composites by Liu *et al.*⁴⁶ We note that we have reported in-plane conductivities due to the relative simplicity of the measurement. Strictly speaking, out-of-plane conductivities are more relevant to rate performance.^{47,48} However, at high loadings the out-of-plane conductivity tends to be ~ 3000 times higher than the in-plane conductivity.⁴⁸ This means the mass fractions (10 and 20%) showing optimised capacity in Fig. 3a will have out-of-plane conductivities approaching 1 S m^{-1} . This is enough to fully maximise rate performance with respect to electrode resistance, as we describe below.⁴⁸

The substantially improved conductive network greatly benefits the composites' capacity and rate performance, as evidenced in Fig. 3a (bottom panel) and Fig. S9 (ESI[†]). For instance, adding 20 wt% CNTs dramatically boosts the capacity from 462 mA h g^{-1} (5 wt% CNT) to 762 mA h g^{-1} at 50 mA g^{-1} , which still maintains 595 mA h g^{-1} as the charge-discharge

rate increased by 40-fold, confirming that the conductive percolated CNT network governs the capacity as well as rate handling properties. Such an effect is even more apparent when normalizing the capacity to InSe mass. As displayed in Fig. 3b, the capacity per InSe in the FL-InSe/CNT composite increases from 486 mA h g^{-1} (5 wt% CNT, 50 mA g^{-1}) to 953 mA h g^{-1} for 20 wt% CNTs. At 2000 mA g^{-1} , the 20 wt% CNT sample still preserves 743 mA h g^{-1} per InSe, and bounces back to 1157 mA h g^{-1} when the current density switches to 50 mA g^{-1} (Fig. 3b), demonstrating excellent reversibility. Apparently, repeated charging-discharging leads to increased capacity per InSe at the 35th cycle compared to that of the 5th cycle. CVs of various thin films are presented in Fig. 3c, showcasing increased integrated area as CNTs are added up to 20%, beyond which it starts to decrease, indicative of an optimum CNT fraction in boosting both capacity and rate performance.

GCD cycling of FL-InSe/CNT films are shown in Fig. 3d and Fig. S10 (ESI[†]). Interestingly, all the films containing CNTs display good cycling performance; increased capacity over cycling is observed, and is CNT content dependent (Fig. 3d). For instance, a 5% CNT composite exhibits a slightly increased capacity after 100 cycles, in sharp contrast to that of a 20% CNT film, whose capacity still climbs up even after 100 cycles. By comparing CVs of 5% and 20% CNT composites at different cycles (Fig. 3e), it is reasonable to deduce that the increase of discharge capacity is mainly due to redox reactions occurring in the potential regime of 0.1–1.5 V (vs. Li/Li⁺). Specifically, reactions in the range 0.1–0.6 V are expected to be responsible for the capacity enhancement, as the partial capacity calculated

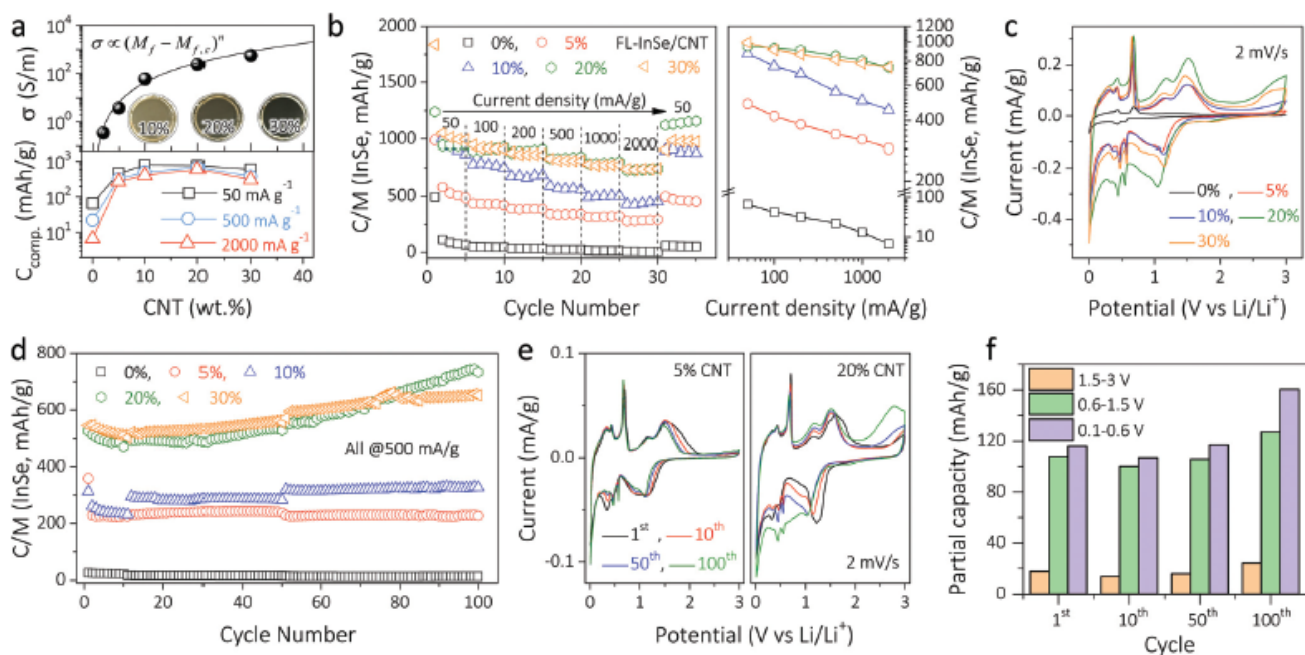
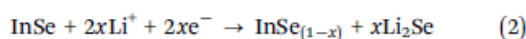


Fig. 3 (a) Electrical conductivity (top panel) and capacity of composite (bottom panel) plotted as a function of CNT mass fraction. Insets in the top panel are optical images of FL-InSe/CNT films with different CNT contents. (b) Rate performance of different composites plotted as a function of cycle number (left panel) and current density (right panel). (c) CV curves at 2 mV s^{-1} and (d) cycling at 500 mA g^{-1} of composites with different CNT contents. (e) CVs of 5% CNT (left) and 20% CNT (right) composite under different number of cycles. (f) Calculated partial discharge capacity within a specific potential regime under different cycles.

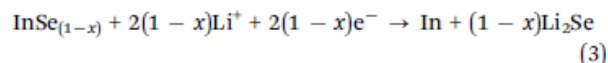
in this potential regime has been improved by 149% from 10th to 100th cycle (Fig. 3f). In addition, peaks at 2.5–3.0 V can be assigned to the conversion of Li_2Se to Se, and is conductivity-dependent. The delithiation kinetics of Li_2Se is facilitated when the conductivity satisfies the charge transfer, thus exhibiting apparent peaks (Fig. 3c), in sharp contrast to the almost negligible peaks in the low-CNT-content electrode (Fig. 3e).

To unveil the reactions in the potential range of interest, we performed *in situ* XRD measurements of the FL-InSe/CNT (20% CNT). The operando results under different cycles are shown in Fig. S11 (ESI[†]). When the cell was firstly discharged from 3 V to 1 V (vs. Li/Li^+), intensity of (004) peak corresponding to InSe decreases while intensity of (111) peak of Li_2Se phase increases (Fig. 4a). No other phase evolutions are observed, suggesting the pristine FL-InSe gradually decomposes into Li_2Se during the first stage lithiation according to reaction (2):

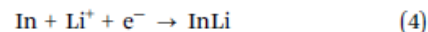


At this stage no evidence of In growing suggests that Se is progressively extracted from InSe in a solid solution process. Upon further lithiation from 1 V to 0.5 V, the (101) peak corresponding to the In phase evolves, coupled with a strengthened

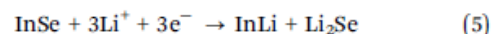
intensity of (111) peak of Li_2Se and the disappearance of the (004) peak of InSe (Fig. 4a), a process that can be described through reaction (3):



When discharged to 0.05 V, (101) peak of In disappears while (111) peak of InLi appears, indicative of alloy reaction through reaction (4):



Thus, in the first discharge process, the hexagonal FL-InSe flakes transform into InLi and Li_2Se following the reaction (5) schematically demonstrated in Fig. 4b and Fig. S12 (ESI[†]):



Along charging to ~ 1 V (Fig. 4c), the (111) and (220) peaks of InLi disappear while (101) peak of In appears in a symmetric way to the discharge process while further charging to 3 V results in shift and reduced intensity of the Li_2Se peak, suggesting the conversion of Li_2Se to Se. At the end of the charge, a mixture of In and Se is obtained, suggesting that the

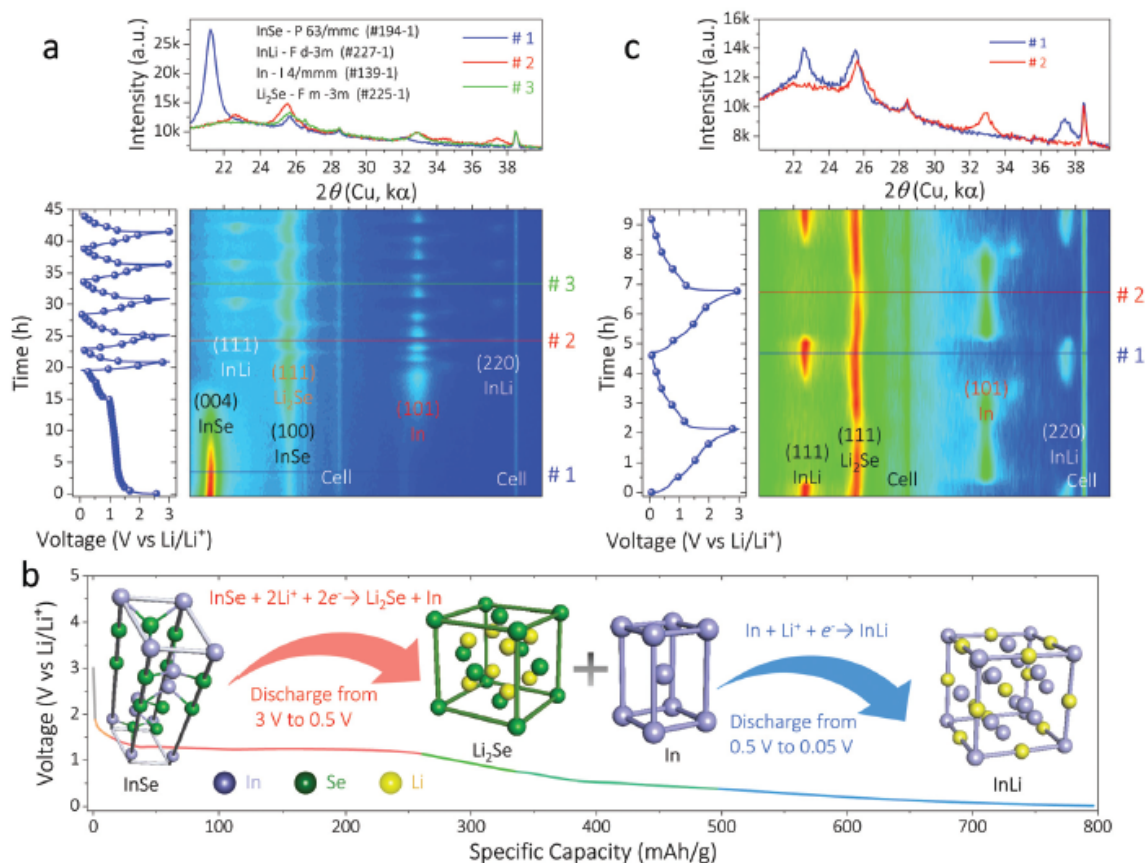
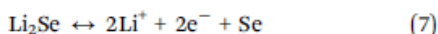
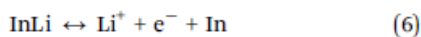


Fig. 4 (a) Contour profiles of *operando* X-ray diffraction patterns from 1st to 5th charge–discharge cycles. (b) Schematic illustration of reactions involved in the first discharge process from 3 V to 0.05 V. (c) Contour profiles of *operando* X-ray diffraction patterns from 8th to 9th charge–discharge cycle. #1, #2, #3 in the bottom panel of a and c represent different charging/discharging states, whose *operando* X-ray diffraction patterns can be found in the top panel of (a) and (c), respectively.

mechanism during charge (delithiation) proceeds in two steps described by the reaction (6) and (7):



Upon 2nd discharge, from 3 V to 1 V, the increased intensity as well as the shift of the (111) peak suggest the conversion from Se to Li_2Se and further discharge to 0.05 V results in decreased intensity of In peaks and growing of InLi (111) peak (Fig. 4c) in a perfect symmetric way as observed during the charge. All extra charge/discharge proceed following the same mechanism showing that once the first cycle leads to irreversibly conversion of InSe to a mixture of In and Li_2Se , the electrochemical process occurs in a fully reversible way, as demonstrated in Fig. S13 (ESI[†]) between a mixture of In/Se and InLi/ Li_2Se in respectively charged and discharged states. The intensity of the In peak (111) also gradually reduced (Fig. 4a and Fig. S13, ESI[†]), which also possibly indicates that the particle size becomes smaller over repeated cycles.

To gain an in-depth understanding of how In atoms accommodate Li^+ , DFT calculations were performed to calculate the adsorption of Li ion on In clusters. The calculated binding

energy for several configurations of cluster including different Li/In and In/ Li_2Se ratio are plotted in Fig. 5a, indicating that indium is indeed capable of forming stable clusters without significantly increasing the binding energy (state 1–4).

We further performed the calculation of absorbed Li amount on an In_5 -based cluster, which is assumed as the preferred structure, as seen in the red lines in Fig. 5a (state 5–8). The binding energy is maintained at about -1.75 eV when one In_5 cluster has twenty Li adsorbed. A higher absorbed Li^+ on the cluster (*i.e.*, $\text{In}_5\text{Li}_{30}$) results in reduced binding energy, suggesting that the adsorption of 6 Li^+ per In_5 cluster is more challenging. The relaxed adsorption configurations and corresponding binding energies of In_3 , In_4 , In_5 , and In_7 cluster with one Li_2Se adsorbed were also calculated (state 9–12) and indicated that In clusters have a high affinity for Se-containing molecules. Therefore, we believe that, after repeated charging/discharging cycles, In particles gradually reduce their domain size and form nanoclusters. These nanoclusters are able to accommodate four Li^+ per atomic In ($\text{In}_5\text{Li}_{20}$) instead of one Li^+ (InLi, reaction #4 and #6) through alloying reaction, as schematically demonstrated in Fig. 5b. We also note that these nanoclusters are highly reactive with electrolyte, contributing a partial of capacity associated with possible electrolyte decomposition like observed

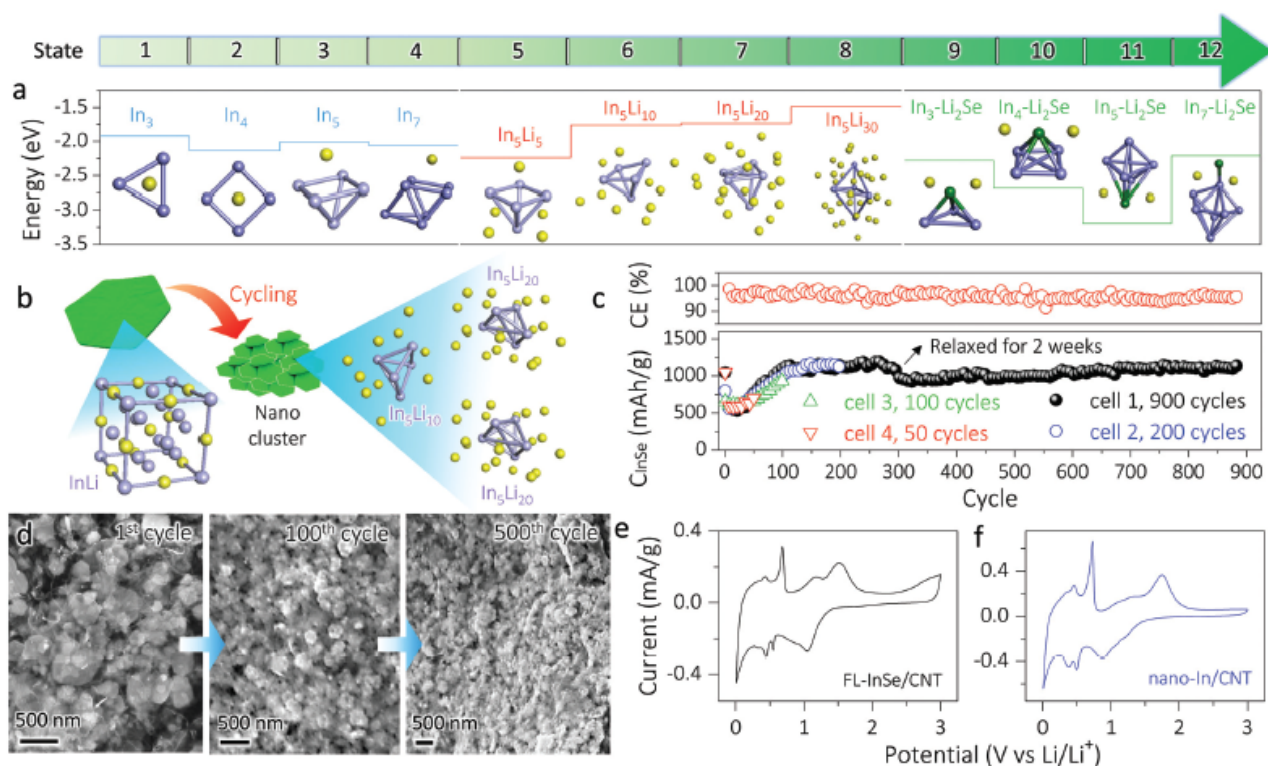


Fig. 5 (a) DFT calculations on the binding energy different In nanoclusters configurations (state 1 to 4), adsorb energy of different amount of Li^+ (state 5 to 8) and Li_2Se (state 9 to 12) toward a In_5 cluster, respectively. Insets are possible configurations under each state, indicating the as-formed In particles are able to form stable clusters. These nanoclusters are able to accommodate 4 Li^+ per In unit, resulting in a much higher Li storage capacity beyond the theoretical value, as schematically illustrated in (b). (c) Long-term cycling of different cells at 500 mA g^{-1} . Cell 1 was cycled 280 times, then relaxed for two weeks and then cycled to 900 times. (d) SEM images of post-cycled FL-InSe/CNT electrodes, showing a gradually reduced particle size as a result of prolonged cycling. CVs of (e) FL-InSe/CNT and (f) nano-In/CNT composites at 2 mV s^{-1} , showing quite similar CV curves and indicating their similar Li storage mechanism.

in other conversion-type anodes.^{35,49} As such, the capacity achieved is somewhat higher than the theoretical capacity.

To check this point, we cycled four different cells for 50, 100, 200 and 900 times, respectively. Fig. 5c indicates that the ever-increasing capacity behavior is observed in all cells in the initial 200 cycles, whose values are quite similar at each cycling stage. The capacity per InSe increases from 520 mA h g⁻¹ to 1224 mA h g⁻¹ after 245 cycles (cell 1). After relaxation for 2 weeks, the capacity of cell 1 still climbs up and reaches 1106 mA h g⁻¹, coupled with a high coulombic efficiency of 97% (Fig. 5c). The capacity of FL-InSe/CNT increases upon cycling phenomenon can also be found in Fig. 2e and 3d, and can be documented by the alloying of the continuously-formed nanoclusters, so-called “nanocluster-alloying” mechanism. To check this point, post-mortem SEM images of different cells suggest the InSe flakes decrease in size upon repeated cycling; hexagonal flakes with well-defined shapes are observed after 1 cycle, then become blurred after 50 cycles and disappear completely after 500 cycles (Fig. 5d and Fig. S14, ESI†). Nanoclusters are found in the SEM image of electrodes after cycling 500 times (Fig. S14c and S15, ESI†), confirming the validation of DFT calculation and indicating the extra capacity originates from the reversible nanocluster-alloying mechanism. That is to say, the *in situ* converted In gradually reduces its particle size, forms nanoclusters and stores much more Li majorly through the alloying process, contributing extra capacity to InSe as a result. This implies that nanosized In is a promising LIB anode material. As such, we examined the CV curves of FL-InSe/CNT and pure nanosized In/CNT (In particle size ~ 60 nm) composites (with same CNT content) at 2 mV s⁻¹. Fig. 5e and f are the 5th CVs of two composite electrodes.

Quite encouragingly, apart from the broad anodic peak at 2.5–3.0 V (*vs.* Li/Li⁺) which is ascribed to the conversion of Li₂Se to Se (reaction (7)), other characteristic CV peaks are very alike, suggesting the same Li storage mechanism and implying that In is a promising LIB anode material. This may inspire future studies on the synthesis of nanosized In with different architectures and state-of-the-art performance, provided that the *in situ* formed nanoclusters are still well percolated in the conductive network.

Conclusions

In summary, we have demonstrated the liquid-phase exfoliation of wet-chemistry-synthesized layered InSe crystals to give few-layered InSe flakes, which were further percolated in CNT conductive networks through a colloidal solution processing approach. Due to shortened Li⁺ diffusion paths and enhanced electron transport kinetics, the binder-free flexible composite exhibits superior electrochemical performance (including high capacity and excellent rate capability) to that of bulk InSe. Importantly, the capacity per InSe of the FL-InSe/CNT composite increases over prolonged cycling up to 1224 mA h g⁻¹ from 520 mA h g⁻¹, which is believed to largely relate to the reversible alloying reaction, as confirmed by the operando X-ray diffraction

results. Combining DFT calculations and post-cycling SEM images, we revealed that the *in situ* formed In particles gradually reduce their domain size, forming nanoclusters upon cycling which are able to accommodate four Li⁺ instead of one per atomic In, and leading to extra capacity as the cycling number is increased. Such a new “nanocluster-alloying” Li storage mechanism may point the way in the exploration of other metal chalcogenides to build new architectures with excellent performance in LIBs, wearable electronics and smart energy storage devices.

Conflicts of interest

There are no conflicts to declare.

Acknowledgements

The manuscript was written by C. F. Z. C. F. Z. designed the project, C. F. Z. and J. N. C. discussed the results. All authors contributed to this work with equally by C. F. Z. and M. L. V. N. and C. F. Z. wish to acknowledge the following funding support: SFI AMBER, SFI PIYRA, ERC StG 2DNanoCaps, ERC PoC 2DUSD, ERC PoC 2DInk, FP7 MC ITN MoWSeS, Horizon2020 NMP Co-Pilot. J. N. C. acknowledges the ERC SEMANTICS and SFI (11/PI/1087) for financial support. Dr N. M. was supported by the SFI under 15/SIRG/3329. Z. L. was supported by the Fundamental Research Funds for the Central Universities (YJ201886) and the National Natural Science Foundation of China (Grant No. 501902215). All authors wish to thank the Advanced Microscopy Laboratory (AML) in CRANN, Trinity College. We thank Dr S. Sonia Jaskaniec for the useful experimental help, Dr Patrick Rozier and Prof. Patrice Simon for useful data discussions.

References

- 1 H. Zhang, Q. Liu, Y. Fang, C. Teng, X. Liu, P. Fang, Y. Tong and X. Lu, *Adv. Mater.*, 2019, **31**, 1904948.
- 2 Y. Lu, J. Wang, S. Zeng, L. Zhou, W. Xu, D. Zheng, J. Liu, Y. Zeng and X. Lu, *J. Mater. Chem. A*, 2019, **7**, 21678–21683.
- 3 C. (John) Zhang, Y. Ma, X. Zhang, S. Abdolhosseinzadeh, H. Sheng, W. Lan, A. Pakdel, J. Heier and F. Nüesch, *Energy Environ. Mater.*, 2020, **3**, 29–55.
- 4 R. F. Service, *Science*, 2019, **366**, 292.
- 5 J.-T. Han, Y.-H. Huang and J. B. Goodenough, *Chem. Mater.*, 2011, **23**, 2027–2029.
- 6 J. B. Goodenough and Y. Kim, *Chem. Mater.*, 2010, **22**, 587–603.
- 7 C. (John) Zhang, S.-H. Park, S. E. O'Brien, A. Seral-Ascaso, M. Liang, D. Hanlon, D. Krishnan, A. Crossley, N. McEvoy, J. N. Coleman and V. Nicolosi, *Nano Energy*, 2017, **39**, 151–161.
- 8 C. (John) Zhang, L. Cui, S. Abdolhosseinzadeh and J. Heier, *InfoMat*, 2020, **2**, 613–638.
- 9 J. Xiong, L. Pan, H. Wang, F. Du, Y. Chen, J. Yang and C. (John) Zhang, *Electrochim. Acta*, 2018, **268**, 503–511.

- 10 H. Tang, W. Li, L. Pan, C. P. Cullen, Y. Liu, A. Pakdel, D. Long, J. Yang, N. McEvoy, G. S. Duesberg, V. Nicolosi and C. J. Zhang, *Adv. Sci.*, 2018, **4**, 1800502.
- 11 S. Abdolhosseinzadeh, R. Schneider, A. Verma, J. Heier, F. Nüesch and C. (John) Zhang, *Adv. Mater.*, 2020, **32**, 2000716.
- 12 P. G. Bruce, B. Scrosati and J.-M. Tarascon, *Angew. Chem., Int. Ed.*, 2008, **47**, 2930–2946.
- 13 Y. Wei, Y. Tao, C. Zhang, J. Wang, W. Qiao, L. Ling and D. Long, *Electrochim. Acta*, 2016, **188**, 385–392.
- 14 C. (John) Zhang, S. H. Park, A. Seral-Ascaso, S. Barwich, N. McEvoy, C. S. Boland, J. N. Coleman, Y. Gogotsi and V. Nicolosi, *Nat. Commun.*, 2019, **10**, 849.
- 15 J. N. Coleman, M. Lotya, A. O'Neill, S. D. Bergin, P. J. King, U. Khan, K. Young, A. Gaucher, S. De, R. J. Smith, I. V. Shvets, S. K. Arora, G. Stanton, H.-Y. Kim, K. Lee, G. T. Kim, G. S. Duesberg, T. Hallam, J. J. Boland, J. J. Wang, J. F. Donegan, J. C. Grunlan, G. Moriarty, A. Shmeliov, R. J. Nicholls, J. M. Perkins, E. M. Grievson, K. Theuwissen, D. W. McComb, P. D. Nellist and V. Nicolosi, *Science*, 2011, **331**, 568–571.
- 16 V. Nicolosi, M. Chhowalla, M. G. Kanatzidis, M. S. Strano and J. N. Coleman, *Science*, 2013, **340**, 1226419.
- 17 D. A. Bandurin, A. V. Tyumina, G. L. Yu, A. Mishchenko, V. Zólyomi, S. V. Morozov, R. K. Kumar, R. V. Gorbachev, Z. R. Kudrynskiy, S. Pezzini, Z. D. Kovalyuk, U. Zeitler, K. S. Novoselov, A. Patané, L. Eaves, I. V. Grigorieva, V. I. Fal'ko, A. K. Geim and Y. Cao, *Nat. Nanotechnol.*, 2017, **12**, 223–227.
- 18 K. Xu, L. Yin, Y. Huang, T. A. Shifa, J. Chu, F. Wang, R. Cheng, Z. Wang and J. He, *Nanoscale*, 2016, **8**, 16802–16818.
- 19 E. Petroni, E. Lago, S. Bellani, D. W. Boukhvalov, A. Politano, B. Gürbulak, S. Duman, M. Prato, S. Gentiluomo, R. Oropesa-Nuñez, J.-K. Panda, P. S. Toth, A. E. Del Rio Castillo, V. Pellegrini and F. Bonaccorso, *Small*, 2018, **14**, 1800749.
- 20 J. Kang, S. A. Wells, V. K. Sangwan, D. Lam, X. Liu, J. Luxa, Z. Sofer and M. C. Hersam, *Adv. Mater.*, 2018, **30**, 1802990.
- 21 M. Li, C.-Y. Lin, S.-H. Yang, Y.-M. Chang, J.-K. Chang, F.-S. Yang, C. Zhong, W.-B. Jian, C.-H. Lien, C.-H. Ho, H.-J. Liu, R. Huang, W. Li, Y.-F. Lin and J. Chu, *Adv. Mater.*, 2018, **30**, 1803690.
- 22 W. Feng, W. Zheng, W. Cao and P. Hu, *Adv. Mater.*, 2014, **26**, 6587–6593.
- 23 S. Lei, F. Wen, L. Ge, S. Najmaei, A. George, Y. Gong, W. Gao, Z. Jin, B. Li, J. Lou, J. Kono, R. Vajtai, P. Ajayan and N. J. Halas, *Nano Lett.*, 2015, **15**, 3048–3055.
- 24 Y.-R. Chang, P.-H. Ho, C.-Y. Wen, T.-P. Chen, S.-S. Li, J.-Y. Wang, M.-K. Li, C.-A. Tsai, R. Sankar, W.-H. Wang, P.-W. Chiu, F.-C. Chou and C.-W. Chen, *ACS Photonics*, 2017, **4**, 2930–2936.
- 25 W.-J. Li, Y.-N. Zhou and Z.-W. Fu, *Appl. Surf. Sci.*, 2011, **257**, 2881–2885.
- 26 S. M. Oh, E. Lee, K. Adpakpang, S. B. Patil, M. J. Park, Y. S. Lim, K. H. Lee, J. Y. Kim and S. J. Hwang, *Electrochim. Acta*, 2015, **170**, 48–56.
- 27 G. Han, Z. G. Chen, D. Ye, B. Wang, L. Yang, Y. Zou, L. Wang, J. Drennan and J. Zou, *J. Mater. Chem. A*, 2015, **3**, 7560–7567.
- 28 Y. Chung and C.-W. Lee, *J. Electrochem. Sci. Technol.*, 2012, **3**, 95–115.
- 29 W. J. Li, Y. N. Zhou and Z. W. Fu, *Appl. Surf. Sci.*, 2011, **257**, 2881–2885.
- 30 K. R. Paton, E. Varrla, C. Backes, R. J. Smith, U. Khan, A. O'Neill, C. Boland, M. Lotya, O. M. Istrate, P. King, T. Higgins, S. Barwich, P. May, P. Puczkarski, I. Ahmed, M. Moebius, H. Pettersson, E. Long, J. Coelho, S. E. O'Brien, E. K. McGuire, B. M. Sanchez, G. S. Duesberg, N. McEvoy, T. J. Pennycook, C. Downing, A. Crossley, V. Nicolosi and J. N. Coleman, *Nat. Mater.*, 2014, **13**, 624–630.
- 31 S. De, P. J. King, M. Lotya, A. O'Neill, E. M. Doherty, Y. Hernandez, G. S. Duesberg and J. N. Coleman, *Small*, 2010, **6**, 458–464.
- 32 G. Cunningham, M. Lotya, C. S. Cucinotta, S. Sanvito, S. D. Bergin, R. Menzel, M. S. P. Shaffer and J. N. Coleman, *ACS Nano*, 2012, **6**, 3468–3480.
- 33 D. Hanlon, C. Backes, E. Doherty, C. S. Cucinotta, N. C. Berner, C. Boland, K. Lee, A. Harvey, P. Lynch, Z. Gholamvand, S. Zhang, K. Wang, G. Moynihan, A. Pokle, Q. M. Ramasse, N. McEvoy, W. J. Blau, J. Wang, G. Abellan, F. Hauke, A. Hirsch, S. Sanvito, D. D. O'Regan, G. S. Duesberg, V. Nicolosi and J. N. Coleman, *Nat. Commun.*, 2015, **6**, 8563.
- 34 A. Harvey, C. Backes, Z. Gholamvand, D. Hanlon, D. McAteer, H. C. Nerl, E. McGuire, A. Seral-Ascaso, Q. M. Ramasse, N. McEvoy, S. Winters, N. C. Berner, D. McCloskey, J. F. Donegan, G. S. Duesberg, V. Nicolosi and J. N. Coleman, *Chem. Mater.*, 2015, **27**, 3483–3493.
- 35 C. J. Zhang, S.-H. Park, O. Ronan, A. Harvey, A. Seral-Ascaso, Z. Lin, N. McEvoy, C. S. Boland, N. C. Berner, G. S. Duesberg, P. Rozier, J. N. Coleman and V. Nicolosi, *Small*, 2017, **13**, 1701677.
- 36 D. McAteer, Z. Gholamvand, N. McEvoy, A. Harvey, E. O'malley, G. S. Duesberg and J. N. Coleman, *ACS Nano*, 2016, **10**, 672–683.
- 37 C. Backes, B. M. Szydłowska, A. Harvey, S. Yuan, V. Vega-Mayoral, B. R. Davies, P.-L. Zhao, D. Hanlon, E. J. G. Santos, M. I. Katsnelson, W. J. Blau, C. Gadermaier and J. N. Coleman, *ACS Nano*, 2016, **10**, 1589–1601.
- 38 C. Backes, R. J. Smith, N. McEvoy, N. C. Berner, D. McCloskey, H. C. Nerl, A. O'Neill, P. J. King, T. Higgins, D. Hanlon, N. Scheuschner, J. Maultzsch, L. Houben, G. S. Duesberg, J. F. Donegan, V. Nicolosi and J. N. Coleman, *Nat. Commun.*, 2014, **5**, 4576.
- 39 S. Mourdikoudis and L. M. Liz-Marzán, *Chem. Mater.*, 2013, **25**, 1465–1476.
- 40 H. P. Kang, K. Jang, S. Kim, J. K. Hae and U. S. Seung, *J. Am. Chem. Soc.*, 2006, **128**, 14780–14781.
- 41 T. Hayashi, K. Ueno, K. Saiki and A. Koma, *J. Cryst. Growth*, 2000, **219**, 115–122.
- 42 J. N. Coleman, *Acc. Chem. Res.*, 2013, **46**, 14–22.
- 43 J. F. Sánchez-Royo, G. Muñoz-Matutano, M. Brotons-Gisbert, J. P. Martínez-Pastor, A. Segura, A. Cantarero, R. Mata, J. Canet-Ferrer, G. Tobias, E. Canadell, J. Marqués-Hueso, B. D. Gerardot and S.-V. Berlin, *Nano Res.*, 2014, **7**, 1556–1568.
- 44 F. Du, H. Tang, L. Pan, T. Zhang, H. Lu, J. Xiong, J. Yang and C. (John) Zhang, *Electrochim. Acta*, 2017, **235**, 690–699.

- 45 D. Stauffer and A. Aharony, *Computer (Long. Beach. Calif.)*, 1994, **1**, 192.
- 46 Y. Liu, X. He, D. Hanlon, A. Harvey, U. Khan, Y. Li and J. N. Coleman, *ACS Nano*, 2016, **10**, 5980–5990.
- 47 R. Tian, S. H. Park, P. J. King, G. Cunningham, J. Coelho, V. Nicolosi and J. N. Coleman, *Nat. Commun.*, 2019, **10**, 1–11.
- 48 R. Tian, N. Alcala, S. J. O'Neill, D. Horvath, J. Coelho, A. Griffin, Y. Zhang, V. Nicolosi, C. O'Dwyer and J. N. Coleman, *ACS Appl. Energy Mater.*, 2020, **3**, 2966–2974.
- 49 S. H. Park, P. J. King, R. Tian, C. S. Boland, J. Coelho, C. (John) Zhang, P. McBean, N. McEvoy, M. P. Kremer, D. Daly, J. N. Coleman and V. Nicolosi, *Nat. Energy*, 2019, **4**, 560–567.